

# A constitutive model for simple shear of dense frictional suspensions

Abhinendra Singh,<sup>1, a)</sup> Romain Mari,<sup>2</sup> Morton M. Denn,<sup>1,3</sup> and Jeffrey F. Morris<sup>1,3</sup>

<sup>1)</sup>*Benjamin Levich Institute, CUNY City College of New York, New York, NY 10031, USA.*

<sup>2)</sup>*Department of Applied Mathematics and Theoretical Physics, Centre for Mathematical Sciences, University of Cambridge, Cambridge CB3 0WA, United Kingdom.*

<sup>3)</sup>*Department of Chemical Engineering, CUNY City College of New York, New York, NY 10031.*

(Dated: 22 August 2017)

Discrete particle simulations are used to study the shear rheology of dense, stabilized, frictional particulate suspensions in a viscous liquid, toward development of a constitutive model for steady shear flows at arbitrary stress. These suspensions undergo increasingly strong continuous shear thickening (CST) as solid volume fraction  $\phi$  increases above a critical volume fraction, and discontinuous shear thickening (DST) is observed for a range of  $\phi$ . When studied at controlled stress, the DST behavior is associated with non-monotonic flow curves of the steady-state stress as a function of shear rate. Recent studies have related shear thickening to a transition between mostly lubricated to predominantly frictional contacts with the increase in stress. In this study, the behavior is simulated over a wide range of the dimensionless parameters ( $\phi$ ,  $\tilde{\sigma}$ , and  $\mu$ ), with  $\tilde{\sigma} = \sigma/\sigma_0$  the dimensionless shear stress and  $\mu$  the coefficient of interparticle friction: the dimensional stress is  $\sigma$ , and  $\sigma_0 \propto F_0/a^2$ , where  $F_0$  is the magnitude of repulsive force at contact and  $a$  is the particle radius. The data have been used to populate the model of the lubricated-to-frictional rheology of Wyart and Cates [Phys. Rev. Lett.**112**, 098302 (2014)], which is based on the concept of two viscosity divergences or “jamming” points at volume fraction  $\phi_J^0 = \phi_{\text{rcp}}$  (random close packing) for the low-stress lubricated state, and at  $\phi_J(\mu) < \phi_J^0$  for any nonzero  $\mu$  in the frictional state; a generalization provides the normal stress response as well as the shear stress. A flow state map of this material is developed based on the simulation results. At low stress and/or intermediate  $\phi$ , the system exhibits CST, and DST appears at volume fractions below but approaching the frictional jamming point. For  $\phi < \phi_J^\mu$ , DST is associated with a material transition from one stress-independent rheology to another, while for  $\phi > \phi_J^\mu$ , the system exhibits DST to shear jamming as the stress increases.

## I. INTRODUCTION

Dense non-Brownian suspensions of rigid particles exhibit diverse rheological behavior, including yielding, shear thinning or shear thickening, normal stress differences, particle migration and shear jamming<sup>1–4</sup>. Shear thickening of dense suspensions is a phenomenon in which, for a range of applied shear stress, the apparent viscosity increases, sometimes by an order of magnitude or more<sup>5–7</sup>. Strong continuous shear thickening (CST) is observed in concentrated suspensions, where the viscosity increases continuously with increase in shear rate. At volume fractions above a critical value an abrupt increase in viscosity may be observed and is termed discontinuous shear thickening (DST).

Recent experimental<sup>8–12</sup> and computational<sup>8,13–17</sup> work has demonstrated that shear thickening (both CST and DST) can arise due to frictional particle-particle contacts. In a suspension, a repulsive force is often present due to steric (e.g. due to adsorbed polymer) or electrostatic stabilization. When the shear forces acting to bring a pair of particles into contact exceed the repulsive force threshold, only fluid mechanical forces are available to keep the particle surfaces apart, and Melrose and Ball<sup>18</sup>

have shown that the lubrication film can go to arbitrarily small values. We therefore assume the lubrication film can break, allowing for contact interactions of both normal and tangential (frictional) form, which most simply can be seen as representative of direct surface contacts due to roughness, but could also be a result of other phenomena, e.g. polymer brush interactions<sup>8</sup>. Thus the repulsive force  $F_0$  gives rise to a stress scale  $\sigma_0 = F_0/6\pi a^2$  for particles of radius  $a$ , which marks a crossover from lubricated (frictionless) contacts between particles to direct, frictional contacts. In an idealized model where stabilization forces themselves do not contribute to the stress and only act as a switch for friction (a realization of which is possible in simulations, see the discussion of the “critical load model”<sup>15</sup>), at low stress ( $\sigma \ll \sigma_0$ ) the particle interactions are lubricated (frictionless) so that the system is rate-independent with the viscosity diverging at the frictionless jamming point  $\phi_J^0$ , corresponding to random close packing of  $\phi_{\text{rcp}} \approx 0.64$  for monodisperse spheres. On the other hand, in the shear-thickened state (for  $\sigma \gg \sigma_0$ ) almost all contacts are frictional, the viscosity is again rate-independent but diverges at a volume fraction  $\phi_J^\mu < \phi_J^0$ , where  $\phi_J^\mu = \phi_J(\mu)$  is used as shorthand to denote the dependence of this jamming fraction on the interparticle friction coefficient  $\mu$ <sup>15,19–22</sup>. With increase in  $\sigma$ , the crossover between these two states results in the shear thickening behavior. At large  $\phi$ , a finite-range stabilizing force becomes one of the major sources of stress

<sup>a)</sup>asingh@ccny.cuny.edu

at low stresses, which leads to a shear-thinning rheology. In this work, we focus on developing a constitutive model for the shear-thickening part of the flow curves. Our proposed model does not include the physics behind the shear-thinning at low stresses, but as this is due to an unrelated microscopic mechanism with its own set of parameters, our idealized model could in principle be augmented to include the relevant low stress physics and display both shear thinning and shear thickening.

Along this line of thought, aspects of which had been developed in Bashkirtseva *et al.*<sup>23</sup>, Wyart and Cates<sup>24</sup> (WC) have shown that under rather broad conditions a viscosity increasing with shear stress by interpolating between two rate-independent asymptotic rheologies can lead to three forms of shear stress curves as a function of shear rate (cf. Fig. 1), depending on the viscosity difference between the two states representative of unthickened and thickened suspensions. When this difference is small, i.e. for  $\phi \ll \phi_j^\mu$ , the shear thickening is continuous, with a monotonic relation between shear stress and rate. For a large enough but finite viscosity contrast, i.e. when  $\phi_c < \phi < \phi_j^\mu$ , the flow curve  $\sigma(\dot{\gamma})$  becomes non-monotonic, S-shaped, and the thickening becomes discontinuous. Finally, when the thickened branch is actually jammed, i.e. for  $\phi \geq \phi_j^\mu$ , the system can flow only for low stresses, while at high stresses frictional contacts cause the system to shear jam, and in this case the flow curve at large stress tends toward a zero shear rate state. Non-monotonic flow curves have been reported under controlled stress conditions in several subsequent experimental and simulation studies<sup>9,16,25,26</sup>.

Wyart and Cates<sup>24</sup> have also proposed a rheological model for shear thickening exhibiting the features noted above. This model is based on an interpolation between two diverging stress-independent rheologies, where the interpolation depends on a unique microscopic state parameter identified as the “fraction of frictional contacts”,  $f$ . Wyart and Cates described  $f$  as a function of  $\Pi$ , the particle pressure, but in standard rheometric experiments, where  $\phi$  is fixed,  $\Pi$  and  $\sigma$  are directly related<sup>27</sup>. Since  $\sigma$  is more readily controlled, we find it more convenient to consider  $f(\tilde{\sigma})$ , where  $\tilde{\sigma} = \sigma/\sigma_0$ . In rate-controlled simulations,  $f$  has been found to be a function of  $\tilde{\sigma}^{15}$ , while in pressure-controlled simulations,  $f$  is not found to be a unique function of  $\Pi^{28}$ . The quantity  $f$  serves, in essence, as an order parameter for the shear thickening transition, assuming low values in the low viscosity state under small stress, and asymptotically approaching  $f \approx 1$  in the large viscosity state at large stress.

In this article, we explore the WC model by comparison to extensive numerical simulations we have performed by varying systematically the volume fraction and friction coefficient of the microscopic model, and exploring the resulting stress (or rate) dependence. Informed by the numerical results, we then introduce empirical expressions for the relations between the parameters  $\mu$ ,  $\phi$ , the order parameter  $f$ , and the steady-state stress. We find that upon increasing the friction coefficient, the frictional

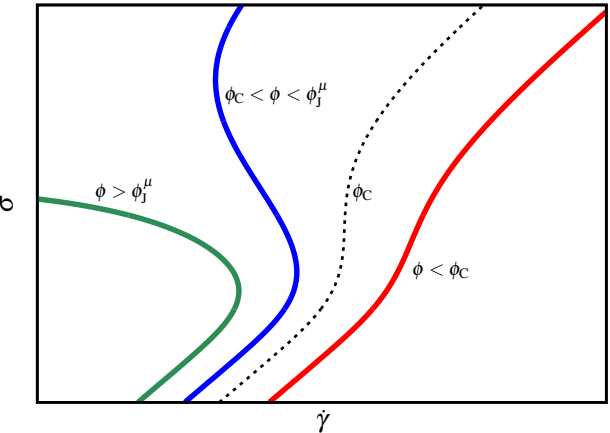


FIG. 1. Sketch of the relation between the shear stress  $\sigma$  and the shear rate  $\dot{\gamma}$  in a shear thickening suspension, with increasing volume fraction  $\phi$  from left to right. For  $\phi < \phi_c$  (dotted line),  $\sigma(\dot{\gamma})$  is monotonic and the shear thickening is continuous.  $\phi = \phi_c$  corresponds to the “critical volume fraction” at which  $\sigma(\dot{\gamma})$  has a point where it shows infinite slope. In the range  $\phi_c < \phi < \phi_j^\mu$ , the flow curve becomes non-monotonic and suspension undergoes discontinuous shear thickening. For  $\phi > \phi_j^\mu$ , the backward bending branch hits the vertical axis. This means that the suspension can flow only at small shear stress.

jamming point  $\phi_j^\mu$  decreases, but the power-law exponent of divergence for both shear and normal stresses,  $\sim (\phi_j - \phi)^{-\beta}$  remains well-described by  $\beta = 2$ . We show that the WC model is highly effective at predicting the shear stress for a wide range of  $\mu$  and  $\phi$ . An extension following the same model structure provides predictions for the normal stress response to allow for a complete description of the viscometric functions in steady simple-shear flow of shear thickening suspensions.

## II. SIMULATION METHODS

We simulate an assembly of inertialess frictional spheres immersed in a Newtonian fluid under an imposed shear stress  $\sigma$ , giving rise to an imposed velocity field  $\mathbf{v} = \dot{\gamma}(t)\hat{\mathbf{v}}(\mathbf{x}) = \dot{\gamma}(t)(x_2, 0, 0)$ . We use Lees-Edwards periodic boundary conditions with  $N = 500$  particles in a unit cell. To avoid ordering, we use bidisperse particles, with radii  $a$  and  $1.4a$  mixed at equal volume fractions. The particles interact through short-range hydrodynamic forces (lubrication), a short-ranged repulsive force and frictional contacts; this simulation model that has been shown to reproduce accurately many features of the experimentally measured rheology for dense shear-thickening suspensions<sup>13,15</sup>, although discrepancies have been noted<sup>29</sup> in the small first normal stress difference relative to some experimental observations<sup>30</sup>.

The equation of motion for  $N$  spheres is the  $6N$ -dimensional force/torque balance between hydrodynamic

$(\mathbf{F}_H)$ , repulsive  $(\mathbf{F}_R)$ , and contact  $(\mathbf{F}_C)$  interactions,

$$\mathbf{0} = \mathbf{F}_H(\mathbf{X}, \mathbf{U}) + \mathbf{F}_C(\mathbf{X}) + \mathbf{F}_R(\mathbf{X}), \quad (1)$$

where the particle positions are denoted by  $\mathbf{X}$  and their velocities/angular velocities by  $\mathbf{U}$ .  $\mathbf{F}_R$  is a conservative force and can be determined based on the positions  $\mathbf{X}$  of the particles, while the calculation of the tangential component of the contact force  $\mathbf{F}_C$  is more involved as it depends on the deformation history of the contact.

We make the translational velocities dimensionless with  $\dot{\gamma}a$  and the shear rate and rotation rates by  $\dot{\gamma}$ . Decomposing the dimensionless velocity as  $\hat{\mathbf{v}}(\mathbf{r}) = \hat{\boldsymbol{\omega}} \times \mathbf{r} + \hat{\mathbf{e}} \cdot \mathbf{r}$  in rotational  $\hat{\boldsymbol{\omega}} = (0, 0, -1/2)$  and extensional  $\hat{\mathbf{e}}_{12} = \hat{\mathbf{e}}_{21} = 1/2$  parts, the hydrodynamic force and torque vector takes the form

$$\mathbf{F}_H(\mathbf{X}, \mathbf{U}) = -\mathbf{R}_{FU}(\mathbf{X}) \cdot (\mathbf{U} - \dot{\gamma}\hat{\mathbf{U}}^\infty) + \dot{\gamma}\mathbf{R}_{FE}(\mathbf{X}) : \hat{\mathbf{E}}, \quad (2)$$

with  $\hat{\mathbf{U}}^\infty = (\hat{\mathbf{v}}(y_1), \dots, \hat{\mathbf{v}}(y_N), \hat{\boldsymbol{\omega}}(y_1), \dots, \hat{\boldsymbol{\omega}}(y_N))$  and  $\hat{\mathbf{E}} = (\hat{\mathbf{e}}(y_1), \dots, \hat{\mathbf{e}}(y_N))$ . The position dependent resistance tensors  $\mathbf{R}_{FU}$  and  $\mathbf{R}_{FE}$  include the “squeeze”, “shear” and “pump” modes of pairwise lubrication<sup>31</sup>, as well as one-body Stokes drag. The occurrence of contacts between particles due, for example, to surface roughness is mimicked by a regularization of the resistance divergence at vanishing interparticle gap  $h_{ij} = 2(r_{ij} - a_i - a_j)/(a_i + a_j)$ : the “squeeze” mode resistance is proportional to  $1/(h + \delta)$ , while the “shear” and “pump” mode resistances are proportional to  $\log(h + \delta)$ <sup>15</sup>. Here we take  $\delta = 10^{-3}$ .

The electrostatic repulsion force is taken to represent a simple electrostatic double layer interaction between particles, with the force decaying exponentially with the interparticle surface separation  $h$  as  $|F_R| = F_0 \exp(-h/\lambda)$ , with a Debye length  $\lambda$ .

Contacts are modeled by linear springs and dashpots. Tangential and normal components of the contact force  $F_C^{(ij)}$  between two particles satisfy Coulomb’s friction law  $|F_{C,t}^{(ij)}| \leq \mu |F_{C,n}^{(ij)}|$ , where  $\mu$  is the interparticle friction coefficient. Some softness is allowed in the contact, but the spring stiffnesses are taken such that the largest particle overlaps do not exceed 3 % of the particle radius during the simulation.

The equation of motion (1) is solved under the constraint of flow at constant shear stress  $\sigma$ . At any time, the shear stress in the suspension is given by

$$\sigma = \Sigma_{12} = \dot{\gamma}\eta_0 \left( 1 + \frac{5}{2}\phi \right) + \dot{\gamma}\eta_H + \sigma_R + \sigma_C \quad (3)$$

where  $\eta_0$  is the suspending fluid viscosity,  $\eta_H \dot{\gamma} = \dot{\gamma}V^{-1}\{(\mathbf{R}_{SE} - \mathbf{R}_{SU} \cdot \mathbf{R}_{FU}^{-1} \cdot \mathbf{R}_{FE}) : \hat{\mathbf{E}}^\infty\}_{12}$  is the contribution of hydrodynamic interactions to the stress, and  $\sigma_{R,C} = V^{-1}\{\mathbf{X}\mathbf{F}_{R,C} - \mathbf{R}_{SU} \cdot \mathbf{R}_{FU}^{-1} \cdot \mathbf{F}_{R,C}\}_{12}$ , where  $\mathbf{R}_{SU}$  and  $\mathbf{R}_{SE}$  are resistance matrices giving the lubrication stresses from the particles velocities and resistance to deformation, respectively<sup>15,32</sup>, and  $V$  is the volume of the

simulation box. Note that the resistance tensors are proportional to the suspending fluid viscosity. At fixed shear stress  $\sigma$  the shear rate  $\dot{\gamma}$  is the dependent variable that is to be determined at each time step by<sup>16</sup>

$$\dot{\gamma} = \frac{\sigma - \sigma_R - \sigma_C}{\eta_0(1 + 2.5\phi) + \eta_H}. \quad (4)$$

The full solution of the equation of motion (1) under the constraint of fixed stress (3) is thus the velocity<sup>16</sup>

$$\mathbf{U} = \dot{\gamma}\hat{\mathbf{U}}^\infty + \mathbf{R}_{FU}^{-1} \cdot (\dot{\gamma}\mathbf{R}_{FE} : \hat{\mathbf{E}}^\infty + \mathbf{F}_R + \mathbf{F}_C). \quad (5)$$

From these velocities, the positions are updated at each time step. Lastly, the unit scales are  $\dot{\gamma}_0 \equiv F_0/6\pi\eta_0 a^2$  for the strain rate and  $\sigma_0 \equiv \eta_0\dot{\gamma}_0 = \frac{F_0}{6\pi a^2}$  for the stress. In the rest of the paper, we use scaled stress defined as  $\tilde{\sigma} = \sigma/\sigma_0$ .

### III. MODEL

In this section we present simulation results for values of friction coefficient  $\mu = 0.1, 0.2, 0.5, 1, 5$ , and  $10$ . As the friction coefficient determines  $\phi_J^\mu$ , the results allow an exploration of the effect of the separation between  $\phi_J^\mu$  and  $\phi_J^0$  on the rheology. As previously shown<sup>19,20,22</sup>,  $0.1 \leq \mu \leq 1.0$  corresponds to the moderate friction limit, where the friction coefficient affects the jamming point  $\phi_J^\mu$ ;  $\mu > 1$  corresponds to large friction, and we find that  $\phi_J^\mu$  saturates rapidly with  $\mu > 1$ .

In the following, the shear stress  $\sigma$ , particle pressure  $\Pi$ , and normal stress differences  $N_1$  and  $N_2$  are defined as  $\sigma \equiv \Sigma_{12}$ ,  $\Pi \equiv -(\Sigma_{11} + \Sigma_{22} + \Sigma_{33})/3$ ,  $N_1 \equiv (\Sigma_{11} - \Sigma_{22})$ , and  $N_2 \equiv (\Sigma_{22} - \Sigma_{33})$ , respectively. All the stress components are non-dimensionalized by  $\eta_0\dot{\gamma}_0$ . The dimensionless particle pressure  $\Pi/\eta_0\dot{\gamma}_0 \equiv \eta_n$  represents the “normal stress viscosity”<sup>27</sup>.

The basic assumption of the model<sup>24</sup> is that  $\eta_r$ ,  $\Pi/\eta_0\dot{\gamma}_0$  and  $N_2/\eta_0\dot{\gamma}_0$  are in distinct stress-independent states both at low ( $\tilde{\sigma} \ll 1$ ) and high ( $\tilde{\sigma} \gg 1$ ) stress. Here we model the  $\phi$  dependence of viscosity and normal stresses as  $(\phi_J - \phi)^{-2}$  and  $\phi^2(\phi_J - \phi)^{-2}$ , respectively. The forms are consistent with the proposed correlations for constant volume<sup>27,33</sup> as well as constant pressure conditions<sup>34</sup>.

The viscosity, particle pressure, and second normal stress difference as functions of  $\phi$  in low and high stress states can be expressed as

$$\eta_r^L(\phi) = \alpha^0(\phi_J^0 - \phi)^{-2} \quad (6a)$$

$$\eta_r^H(\phi, \mu) = \alpha^\mu(\phi_J^\mu - \phi)^{-2}, \quad (6b)$$

$$\frac{\Pi^L}{\eta_0\dot{\gamma}}(\phi) = \beta^0\phi^2(\phi_J^0 - \phi)^{-2}, \quad (6c)$$

$$\frac{\Pi^H}{\eta_0 \dot{\gamma}}(\phi, \mu) = \beta^\mu \phi^2 (\phi_J^\mu - \phi)^{-2} , \quad (6d)$$

$$\frac{N_2^L}{\eta_0 \dot{\gamma}}(\phi) = K_2^0 \phi^2 (\phi_J^0 - \phi)^{-2} , \quad (6e)$$

$$N_2^H / \eta_0 \dot{\gamma}(\phi, \mu) = K_2^\mu \phi^2 (\phi_J^\mu - \phi)^{-2} , \quad (6f)$$

where  $\alpha^{0,\mu}$ ,  $\beta^{0,\mu}$ ,  $K_2^{0,\mu}$  are constant coefficients. Recall that  $\phi_J^0$  and  $\phi_J^\mu$  denote the jamming volume fraction for  $\mu = 0$  (frictionless state) and nonzero values of  $\mu$  (frictional states), respectively. Different functional forms for shear stress and particle pressure (note the leading  $\phi^2$  term in (6c)) leads to a stress ratio  $\mu_{\text{bulk}} = \sigma/\Pi$  (or  $q = \Pi/\sigma$  in suspension flow modeling<sup>27</sup>) being volume fraction dependent, consistent with the experimental results of Boyer *et al.*<sup>34</sup>.

The friction-dependent parameters are found empirically from our simulations to be expressible as functions of  $\mu$ :

$$\phi_J(\mu) = \phi_J^0 - (\phi_J^0 - \phi_J^\infty) \exp(-\mu_\phi/\mu) , \quad (7a)$$

$$\alpha(\mu) = \alpha^0 + (\alpha^\infty - \alpha^0) \exp(-\mu_\alpha/\mu) , \quad (7b)$$

$$\beta(\mu) = \beta^0 + (\beta^\infty - \beta^0) \exp(-\mu_\alpha/\mu) , \quad (7c)$$

$$K_2(\mu) = K_2^0 + (K_2^\infty - K_2^0) \exp(-\mu_\alpha/\mu) \quad (7d)$$

as shown by the fits in Fig. 3. The fitting parameters  $\mu_\phi$  and  $\mu_\alpha$  are reported in table I; note that this table contains all friction-independent parameters of the model.

Next, we specify the flow curves utilizing a stress-dependent jamming volume fraction, using an expression similar to that proposed by Wyart and Cates<sup>24</sup>

$$\phi_m(\tilde{\sigma}, \mu) = \phi_J(\mu) f(\tilde{\sigma}) + \phi_J^0 [1 - f(\tilde{\sigma})] , \quad (8a)$$

where  $f(\tilde{\sigma})$  denotes the fraction of close particle interactions in which shear forces have overcome the stabilization repulsive force  $F_0$  to achieve contact. We propose stress-dependent coefficients

$$\alpha_m(\tilde{\sigma}, \mu) = \alpha(\mu) f(\tilde{\sigma}) + \alpha^0 (1 - f(\tilde{\sigma})) , \quad (8b)$$

$$\beta_m(\tilde{\sigma}, \mu) = \beta(\mu) f(\tilde{\sigma}) + \beta^0 (1 - f(\tilde{\sigma})) . \quad (8c)$$

$$K_m(\tilde{\sigma}, \mu) = K_2(\mu) f(\tilde{\sigma}) + K_2^0 (1 - f(\tilde{\sigma})) . \quad (8d)$$

Finally, using (6), (7), and (8) we propose the dependences of the rheological functions on  $\tilde{\sigma}$ ,  $\phi$ , and  $\mu$ :

$$\eta_r(\phi, \tilde{\sigma}, \mu) = \alpha_m(\tilde{\sigma}, \mu) [\phi_m(\tilde{\sigma}, \mu) - \phi]^{-2} , \quad (9a)$$

$$\frac{\Pi}{\eta_0 \dot{\gamma}}(\phi, \tilde{\sigma}, \mu) = \beta_m(\tilde{\sigma}, \mu) \phi^2 [\phi_m(\tilde{\sigma}, \mu) - \phi]^{-2} , \quad (9b)$$

$$\frac{N_2}{\eta_0 \dot{\gamma}}(\phi, \tilde{\sigma}, \mu) = K_m(\tilde{\sigma}, \mu) \phi^2 [\phi_m(\tilde{\sigma}, \mu) - \phi]^{-2} . \quad (9c)$$

The divergences of the rheological functions described above – viscosity,  $N_2$ , and  $\Pi$  – have the same algebraic sign at low and high stress. By contrast,  $N_1$  presents a special case, in that it appears to have different signs under conditions dominated by lubrication and friction<sup>35–38</sup>. We model  $N_1$  as

$$\frac{N_1^L}{\eta_0 \dot{\gamma}}(\phi) = -K_1^0 \phi^2 (\phi_J^0 - \phi)^{-2} \quad (10a)$$

$$\frac{N_1^H}{\eta_0 \dot{\gamma}}(\phi) = K_1(\mu) \phi^2 (\phi_J(\mu) - \phi)^{-2} \quad (10b)$$

Now the stress-and volume fraction-dependent  $N_1$  can be written as

$$\frac{N_1}{\eta_0 \dot{\gamma}}(\tilde{\sigma}, \phi) = K_1^m(\tilde{\sigma}) \phi^2 [\phi_m(\tilde{\sigma}) - \phi]^{-2} , \quad (11a)$$

where  $K_1^m(\tilde{\sigma})$  is given by

$$K_1^m(\tilde{\sigma}) = K_1(\mu) f(\tilde{\sigma}) - K_1^0 (1 - f(\tilde{\sigma})) . \quad (11b)$$

The transition between the lubricated and frictionally dominated stress states is captured by the fraction of frictional interactions,  $f(\tilde{\sigma})$ , which we model as  $f(\tilde{\sigma}) = \exp[-\tilde{\sigma}^*/\tilde{\sigma}]$ , with  $\sigma^* = 1.45\sigma_0$  based on simulations here and previously published results<sup>10,15,17,26,39</sup>. We assume that  $f(\tilde{\sigma})$  does not depend on  $\mu$ .

## IV. RESULTS

Before turning to stress dependence, we show in Fig. 2 our simulation results for the stress-independent  $\eta_r$ ,  $\Pi$  and  $N_2$  for rate-independent states. These agree well with (6) for all values of  $\mu$ . The viscosity at large  $\phi$  is well represented by  $(\phi_J - \phi)^{-2}$  independent of  $\mu$ , as shown in Fig. 2b;  $\phi_J$  is obtained by a least-squares fit of (6a) and (6b) to the volume fraction dependence of the viscosity at low ( $0.1 < \tilde{\sigma} < 0.3$ ) and high ( $\tilde{\sigma} > 10$ ) stresses, respectively.

The friction-dependent constants are found to fit well to exponential functions of the form proposed in (7) as shown in Fig. 3; values of these parameters are presented in the Table I. Because  $N_1$  proves more difficult to reliably simulate (or experimentally measure<sup>30,40,41</sup>), we defer its consideration to a later section.

### A. Rate dependent viscosity

To develop a sense of the entire flow behavior, we present in Fig. 4 the viscosity data with interparticle friction coefficient  $\mu = 1$ . This value of  $\mu$  is comparable to

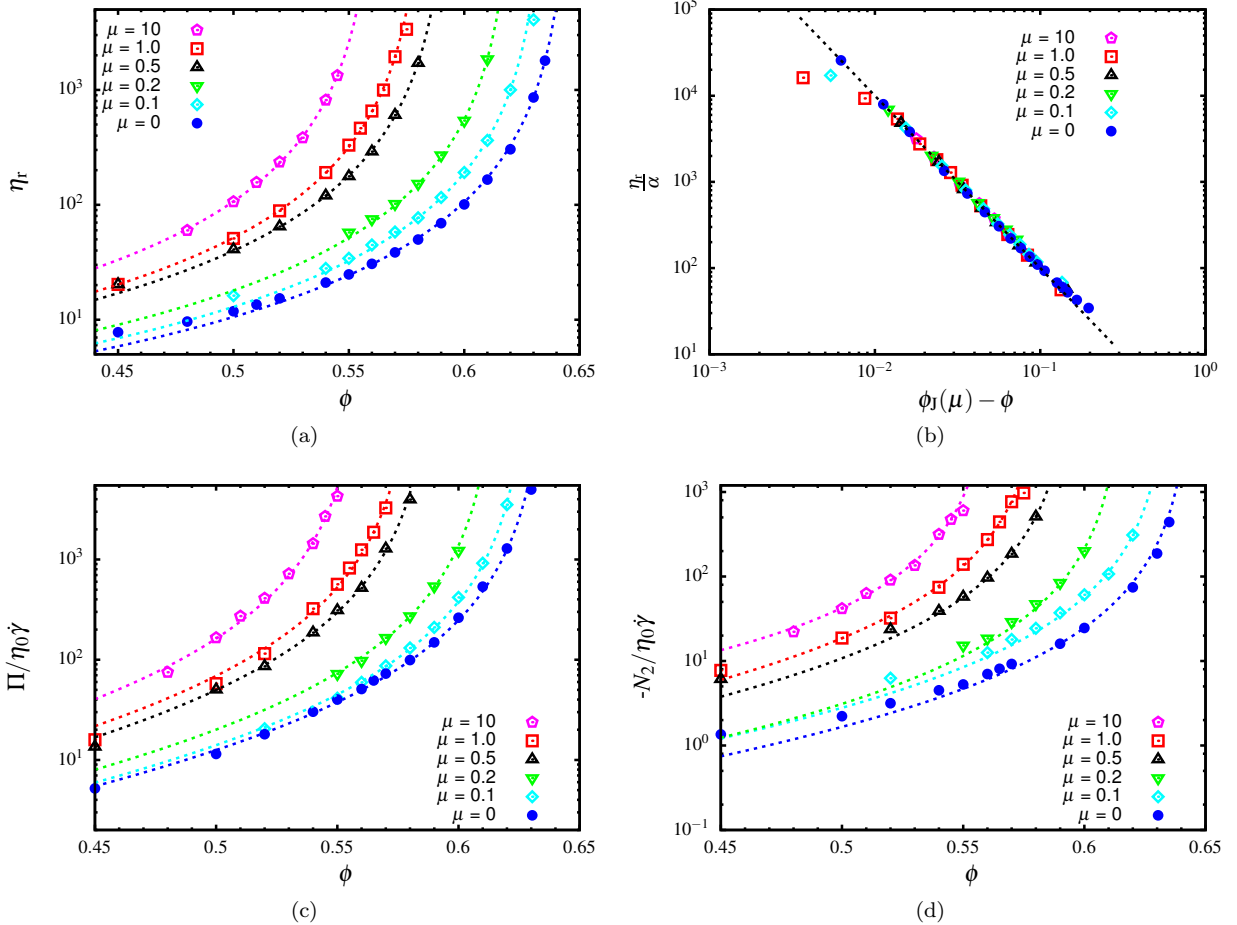


FIG. 2. (a)  $\eta_r(\phi)$ , (c)  $\Pi/\eta_0\dot{\gamma}(\phi)$  and (d)  $N_2/\eta_0\dot{\gamma}(\phi)$  for the rate-independent frictionless (low stress  $0.1 < \tilde{\sigma} < 0.3$ ) and frictional (high stress  $\tilde{\sigma} > 10$ ) states from simulations, with different values of  $\mu$  in the frictional case. Filled symbols represent the frictionless state, while open symbols represent different interparticle friction coefficients. Dashed lines in (a), (c) and (d) are fit to (6). (b) Logarithmic plot of  $\frac{\eta_r}{\alpha}$  versus  $(\phi_J(\mu) - \phi)$  for different values of  $\mu$ . The dashed line is a guide to eye and shows power law -2.

TABLE I.  $\mu$  independent model constants

$\phi_J^0$	$\phi_J^\infty$	$\alpha^0$	$\alpha^\infty$	$\beta^0$	$\beta^\infty$	$K_2^0$	$K_2^\infty$	$\mu_\phi$	$\mu_\alpha$	$K_1^0$
0.646	0.562	0.225	0.510	0.95	2.25	0.18	0.61	0.61	0.24	0.275

the experimentally measured values of Fernandez *et al.*<sup>8</sup>, where  $\mu$  is in the range 0.6–1.1 for polymer brush-coated quartz particles of diameter  $2a \sim 10 \mu\text{m}$ , but is higher than the value of 0.5 reported by Comtet *et al.*<sup>12</sup>. The data are presented in the forms  $\dot{\gamma}(\tilde{\sigma})/\dot{\gamma}_0$ ,  $\eta_r(\dot{\gamma}/\dot{\gamma}_0)$ , and  $\eta_r(\tilde{\sigma})$  for a range of values of  $\phi \geq 0.45$ . Figure 4a shows that for volume fractions  $\phi < 0.56$  the  $\dot{\gamma}(\tilde{\sigma})/\dot{\gamma}_0$  curves are monotonic and show continuous shear thickening for  $0.3 \leq \tilde{\sigma} \leq 10$ . At  $\phi = 0.56$ , the curve exhibits the first sign of non-monotonicity: we define  $\phi_C \doteq 0.56$  to signify the DST onset volume fraction. For  $\phi = 0.57$  and  $\phi = 0.58$ , the slope is negative (i.e.,  $d\dot{\gamma}/d\tilde{\sigma} < 0$ ) for intermediate stress but crosses over to a positive slope for

$\tilde{\sigma} > 10$ , corresponding to the S-shaped  $\eta_r(\dot{\gamma}/\dot{\gamma}_0)$  curves shown in Fig. 4b. The viscosity as modeled by (9a) is shown by solid lines and agrees with the simulation data except at high stresses at  $\phi = 0.58$ . This discrepancy is due to the closeness to  $\phi_J(\mu)$  given by (7a), which slightly underestimates the jamming volume fraction for  $\mu = 1$ .

Although plotted as a function of shear rate, it is important to note that these simulations were performed at fixed shear stress: DST would be observed at fixed rate for this range of volume fraction ( $0.56 \leq \phi \leq 0.58$ ) as S-shaped curves are not accessible in a rate-controlled scenario<sup>16,24</sup>. For this range of  $\phi$ , where DST is observed between two *flowing* states, we term the discon-

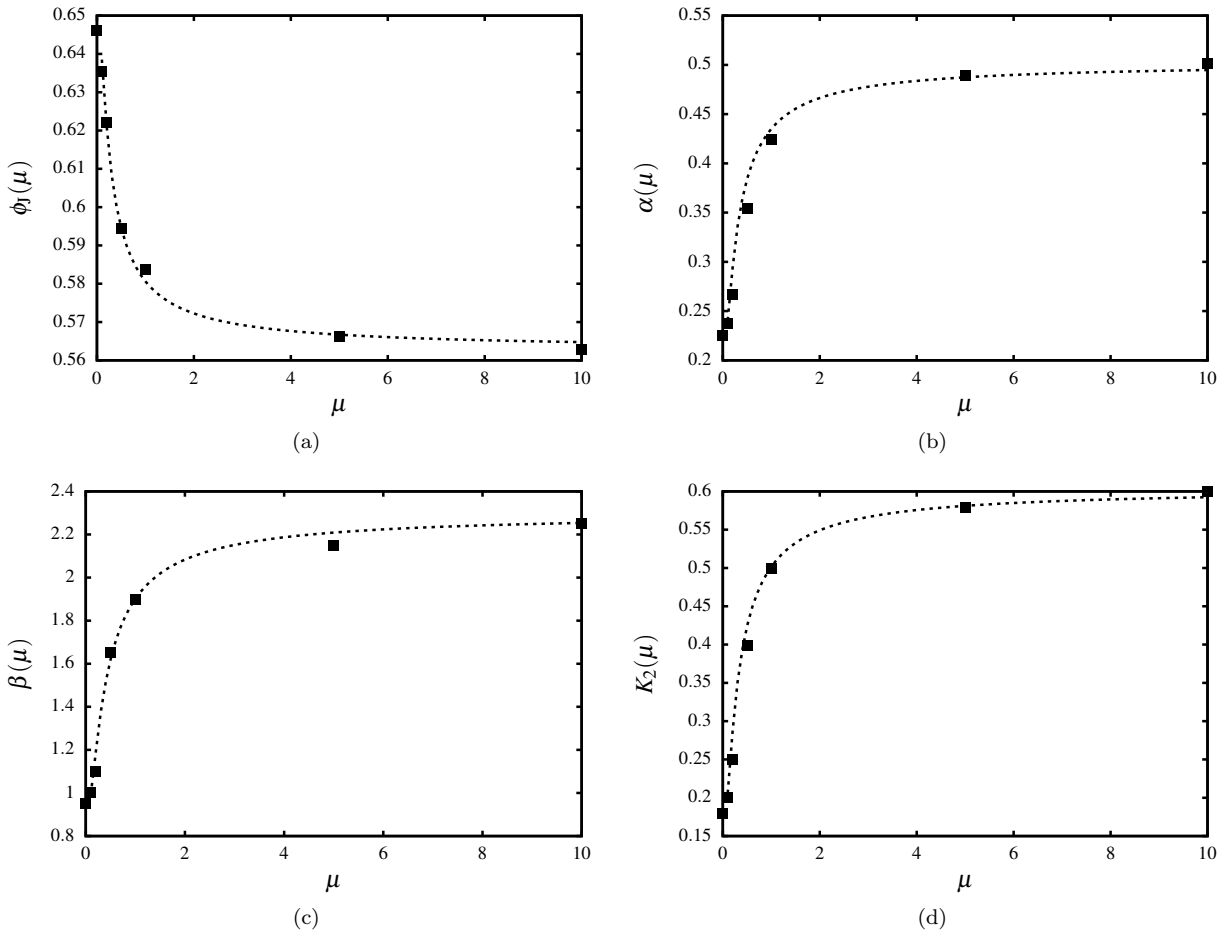


FIG. 3. (a) Jamming volume fraction  $\phi_J(\mu)$  (square) plotted as a function of  $\mu$ . Other friction dependent constants (b)  $\alpha(\mu)$ , (c)  $\beta(\mu)$  and (d)  $K_2(\mu)$  plotted as a function of  $\mu$ . Dashed lines in (a), (b), (c), and (d) are best fits of the data to (7a), (7b), (7c), and (7d) respectively.

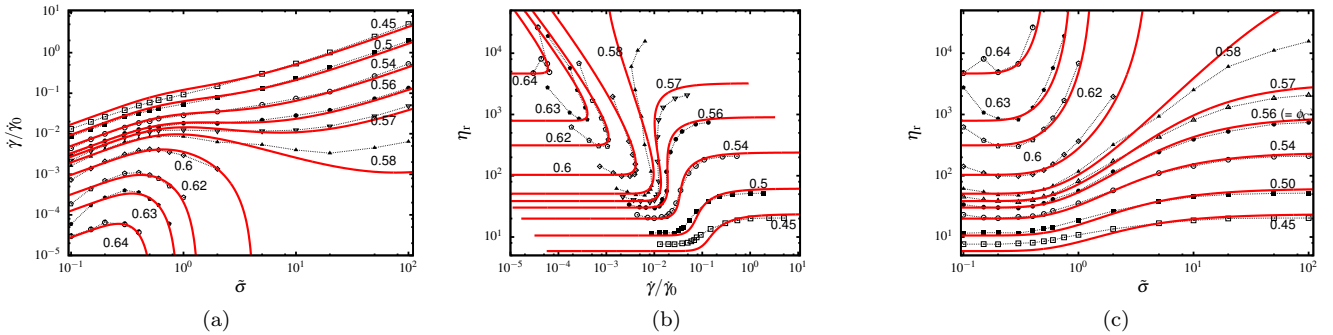


FIG. 4. Steady state flow curves for several values of volume fraction  $\phi$  at  $\mu = 1$ . (a) The dimensionless rate  $\dot{\gamma}/\dot{\gamma}_0$  as a function of dimensionless applied stress  $\tilde{\sigma}$ . Continuous shear thickening (CST) observed at low volume fraction ( $\phi < 0.56$ ) is associated with monotonic flow curves, discontinuous shear thickening (DST) appears as non-monotonic flow curves for  $0.56 \leq \phi \leq 0.58$ , and for  $\phi \geq 0.59$  the system is shear jammed at high stress. (b) The same data plotted as  $\eta_r(\dot{\gamma}/\dot{\gamma}_0)$  flow curve. (c) Relative viscosity  $\eta_r$  as a function of dimensionless applied stress  $\tilde{\sigma}$ . The symbols are simulation data with dashed lines provided to guide the eye. The solid lines are predictions from (9a).

tinuous shear thickening as “pure DST”. However for  $\phi \geq 0.59$ , the upper, i.e. high stress, branch of the S-shaped  $\dot{\gamma}(\tilde{\sigma})$  curves (Fig. 4a) is not accessible, signifying that the suspension enters a shear jammed (SJ) state above  $\tilde{\sigma}_J(\phi)$ . The suspension is flowable for low stress, but is jammed for  $\tilde{\sigma} > \tilde{\sigma}_J(\phi)$ ;  $\tilde{\sigma}_J(\phi)$  decreases with increasing  $\phi$ . We term such discontinuous shear thickening, in which the thickening continues until reaching a shear-jammed state, as “DST-SJ”. When the traditional flow curve  $\eta_r(\dot{\gamma}/\dot{\gamma}_0)$  is plotted for the same data in Fig. 4b, we observe non-monotonicity for  $\phi \geq 0.56$ . This data, when presented in the form  $\eta_r(\tilde{\sigma})$ , shows that the onset stress for shear thickening  $\tilde{\sigma}_{ST} \approx 0.3$  is roughly independent of volume fraction, as observed in previous studies<sup>7,15,42,43</sup>. To characterize shear thickening as CST or DST, we fit  $\eta_r(\tilde{\sigma})$  in the thickening regime to  $\eta_r \sim \tilde{\sigma}^\zeta$ :  $\zeta < 1$  implies continuous shear thickening, while  $\zeta = 1$  implies the onset of DST, and larger  $\zeta$  are in the DST region. We also observe some shear thinning at low stress as a result of the short-range electrostatic repulsion<sup>15</sup>.

The viscosity obtained from (9) is shown in Fig. 5 along with simulation data for different values of  $\mu$ . The model is in excellent agreement with the data. The phenomenology is the same for any value of  $\mu$  except for  $\mu = 0$ . With increasing  $\mu$ , the DST onset volume fraction  $\phi_C$  decreases.

## B. Flow state diagram

The shear rheology described above is controlled by three dimensionless parameters, namely the solid volume fraction  $\phi$ , dimensionless shear stress  $\tilde{\sigma}$ , and interparticle friction coefficient  $\mu$ .

The results discussed are presented in a flow state diagram. As this depends on three variables, we present two views: in the  $\phi$  -  $\tilde{\sigma}$  plane for  $\mu = 1$ , and in the  $\mu$  -  $\phi$  plane for stress  $\tilde{\sigma}_C$ . Figure 6a displays the observed flow state diagram in the  $\phi$  -  $\tilde{\sigma}$  plane, and here we identify three volume fractions:  $\phi_C$ ,  $\phi_J(\mu)$ , and  $\phi_J^0$ . Vertical lines represent frictional  $\phi_J(\mu)$  and frictionless  $\phi_J^0$  jamming points. In the lower part of the diagram, where the stress is too low to overcome the interparticle repulsive force, friction between close particles is not activated and hence the rheology diverges at  $\phi_J^0$ . However, in the upper part of the flow state diagram where the stress is large most of the close interactions (or “contacts”) are frictional which leads to divergence of viscosity and other rheological functions at  $\phi_J(\mu) < \phi_J^0$ . In the two extremes, the viscosity in the model is rate independent. However, in the simulations at low stress, the finite range of repulsion leads to a larger apparent particle size, and the competition between short-range repulsion and external applied stress creates a shear thinning behavior, at the conditions indicated by the + symbols. For intermediate stress, continuous shear thickening is observed in the range of  $\phi < \phi_C$ . For  $\phi_C \leq \phi < \phi_J(\mu)$ , “pure DST” is observed (shown by triangles). In this range of  $\phi$ , the

dashed line is the envelope of the pure DST states, with  $(\phi_C, \tilde{\sigma}_C)$  being the point with the minimum  $\phi$  value along this line. This line is determined as the locus of points for which  $d\dot{\gamma}/d\tilde{\sigma} = 0$  in a flow curve  $\dot{\gamma}(\tilde{\sigma})$  as shown in Fig. 4a: there are two such points on a curve for any  $\phi > \phi_C$  and coalescence of these two points occurs at a critical point  $(\phi_C, \tilde{\sigma}_C)$ .

For  $\phi > \phi_J(\mu)$ , the upper boundary of DST states is the stress-dependent jamming line  $\phi_m(\tilde{\sigma})$ . The jamming line separates the DST regime (diamonds) from conditions yielding a solid-like shear-jammed state (squares). The distinction between two types of DST regimes is based on differences in the high stress state, which is flowable in the pure DST regime (for  $\phi_C \leq \phi < \phi_J(\mu)$ ) and jammed for DST-SJ (for  $\phi_J(\mu) \leq \phi < \phi_J^0$ ). The minimum stress required to observe DST and shear-jammed (SJ) states decreases with increasing  $\phi$ , and eventually these curves converge and the minimum stress for jamming tends to zero as the frictionless jamming point  $\phi_J^0$  is approached.

Figure 6b displays the flow state diagram in the  $\mu$  -  $\phi$  plane for a constant stress  $\tilde{\sigma}_C$ , the minimum stress for DST; we note that  $\tilde{\sigma}_C$  is roughly independent of  $\mu$ . Here, we see a demonstration of how the volume fractions  $\phi_C$ ,  $\phi_J(\mu)$ , and  $\phi_m(\tilde{\sigma}_C)$  decrease as a function of  $\mu$ . The region enclosed between  $\phi_C$  and  $\phi_J(\mu)$  broadens at larger  $\mu$ , illustrating that the range of  $\phi$  over which “pure DST” is observed broadens with increasing interparticle friction. For the range of volume fractions  $\phi_J(\mu) < \phi < \phi_m(\tilde{\sigma}_C)$ , the suspension is in the DST-SJ region, and above  $\phi_m(\tilde{\sigma}_C)$ , the system is in shear-jammed state at the imposed stress.

## C. Rate dependent normal stresses

The simulation data along with the model predictions for the particle pressure  $\Pi/\eta_0\dot{\gamma}$  and second normal stress difference  $N_2/\eta_0\dot{\gamma}$ , are presented in Fig. 7. The proposed model is in good agreement with the simulations. We observe that  $N_2/\eta_0\dot{\gamma}$  is always negative, and is comparable to but smaller than  $\eta_r$ . For volume fraction  $\phi \leq 0.45$ ,  $\Pi/\eta_0\dot{\gamma}$  is smaller than  $\eta_r$ . With increasing  $\phi$  the particle pressure increases faster than the shear stress, and for  $\phi$  approaching  $\phi_J(\mu)$ ,  $\Pi/\eta_0\dot{\gamma}$  becomes larger than the relative viscosity  $\eta_r$ , as deduced in modeling based in part on particle migration data by Morris and Boulay<sup>27</sup>. The experimental data by Boyer *et al.*<sup>34</sup> also show similar decrease in bulk friction coefficient as the jamming volume fraction is approached.

Finally,  $N_1/\eta_0\dot{\gamma}$  from (11) is shown in Fig. 8. Figure 8a displays the divergences of  $N_1/\eta_0\dot{\gamma}$  in stress-independent states, where we choose the divergent volume fraction to be the same as that of  $\eta_r$  for  $\mu = 1$ , where  $K_1^0 = 0.055$  and  $K_1(\mu) = 0.045$  are used. The predictions of the model for the stress-dependent  $N_1/\eta_0\dot{\gamma}$  are plotted along with the simulation data in Figs. 8b and 8c. The modelled  $N_1/\eta_0\dot{\gamma}$  exhibits several features: for all volume fractions

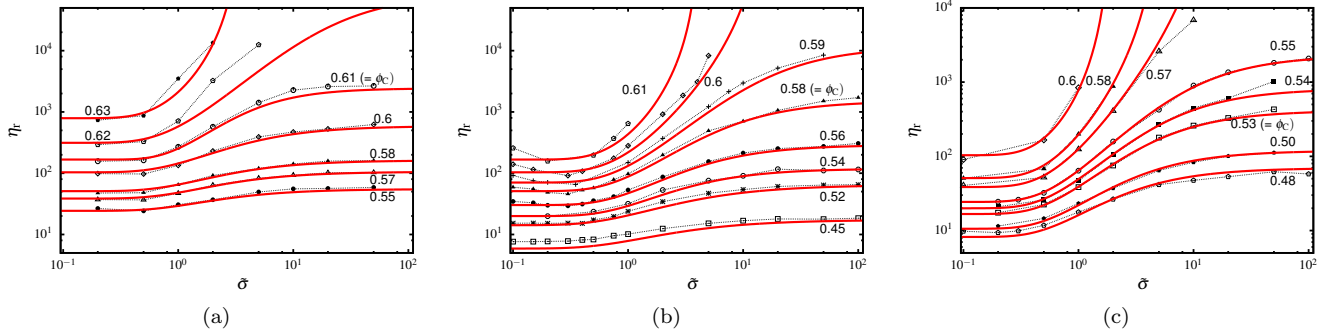


FIG. 5. Varying friction coefficient: steady state relative viscosity  $\eta_r$  plotted against scaled applied stress  $\tilde{\sigma} = \sigma/\sigma_0$  for friction coefficient  $\mu =$  (a) 0.2, (b) 0.5 and (c) 10 for several values of volume fractions as mentioned.  $\phi_C$  denotes the volume fraction for the onset of DST. Symbols and dashed lines indicate the simulation data while solid lines are predictions from (9a).

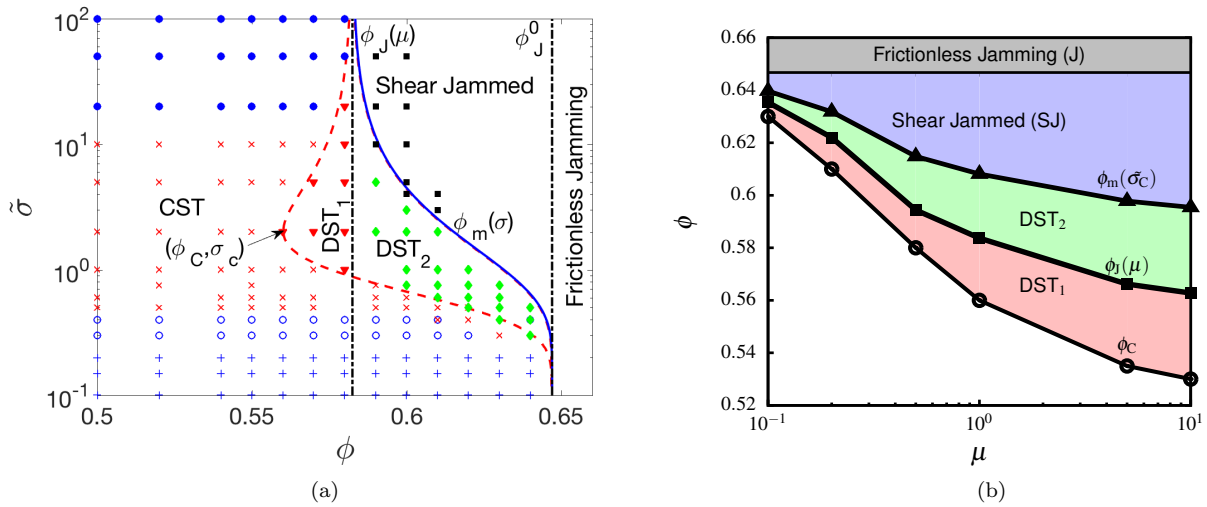


FIG. 6. Flow state diagram  $\tilde{\sigma}, \phi, \mu$  shown in two different projections: (a)  $\phi - \tilde{\sigma}$  plane for a constant interparticle friction  $\mu = 1.0$ . The blue solid line is the stress dependent jamming line  $\phi_m(\tilde{\sigma})$ , while the dashed red line is the DST line and shows locus of points where  $\frac{d\gamma}{d\sigma} = 0$ . Dot-dashed black lines represent  $\phi_J(\mu)$  and  $\phi_J^0$ . Symbols represent different states of the suspension: shear thinning (blue plus), rate-independent (blue circles), continuous shear thickening (red crosses), pure DST (red diamonds), DST-SJ (green diamonds) and shear jammed states (black squares). Along the  $\phi$  axis, there are three special densities:  $\phi_C$  below which there is no DST region,  $\phi_J(\mu)$ , below which there is no shear jamming, and  $\phi_J^0$ , above which isotropically jammed states exist. Corresponding to  $\phi_C$ , DST exists for only one value of stress  $\tilde{\sigma}_C$ , while for  $\phi > \phi_C$  DST exists for a range of stress values. (b)  $\mu - \phi$  plane for a constant stress  $\tilde{\sigma}_C$ . Circles represent the DST onset volume fraction  $\phi_C$ , squares represent frictional jamming point  $\phi_J(\mu)$ , triangles show  $\phi_m(\tilde{\sigma}_C)$ . In between  $\phi_C$  and  $\phi_J(\mu)$  pure DST is observed, while the green region between  $\phi_J(\mu)$  and  $\phi_m(\tilde{\sigma}_C)$  DST-SJ is observed. In the blue region above  $\phi_m(\tilde{\sigma}_C)$ , the suspension is in a shear-jammed state.

$\phi$ ,  $N_1/\eta_0\dot{\gamma}$  is small and negative at small stress, and becomes increasingly negative with increasing stress, reaching a minimum value for  $\tilde{\sigma} \approx 1$ . The magnitude of this negative  $N_1/\eta_0\dot{\gamma}$  becomes larger as  $\phi$  is increased. At stress values  $\tilde{\sigma} > 1$ ,  $N_1(\sigma)/\eta_0\dot{\gamma}$  tends toward positive values, crossing zero at  $\tilde{\sigma}_p$ . The proposed model is in good agreement with the simulation data for the range of volume fraction  $\phi \geq 0.54$ , where the simulation data show positive  $N_1$  at high stress. On the other hand, for volume fraction  $\phi < 0.54$ , the model does not agree with the data at high stress where simulations show negative  $N_1$ , while the model predicts  $N_1$  to be positive. The simula-

tion data and model predictions for  $N_1$  at larger  $\phi$  agree in being negative at small stress (where lubrication films between most particles remain) and becoming positive at large stress (where most of the contacts are frictional). This also agrees in part with observations of Lootens *et al.*<sup>41</sup>, Dbouk *et al.*<sup>44</sup>, and Royer *et al.*<sup>39</sup>, but not with the data of Cwalina and Wagner<sup>30</sup>. However, at lower volume fractions, experiments which have shown  $N_1 < 0$  for all stresses<sup>30,39,41</sup> are in agreement with our simulations, but are not captured by the model. This suggests that there is a difference in microstructure between the lower and higher particle fractions such that behavior consis-

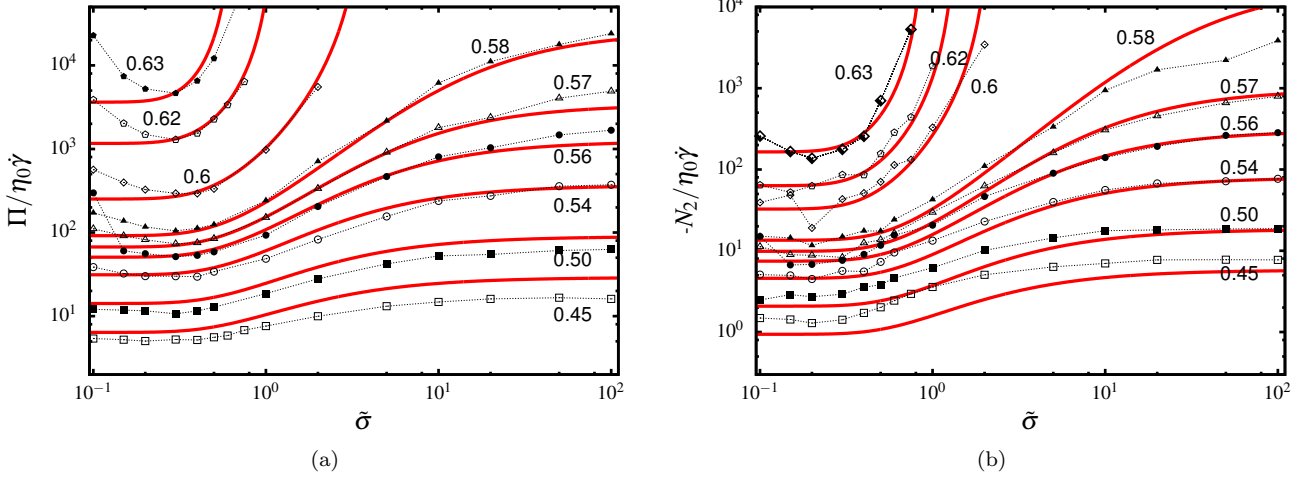


FIG. 7. Steady state (a) particle pressure  $\Pi/\eta_0\dot{\gamma}$ , and (b) second normal stress difference  $N_2/\eta_0\dot{\gamma}$  plotted against applied stress  $\tilde{\sigma} = \sigma/\sigma_0$  for  $\mu = 1$ . Symbols and dashed lines indicate the simulation data while solid lines are predictions from (9b) and (9c).

tent with the lubricated regime is observed in the lower- $\phi$  suspension even when contacts are frictional.

## V. DISCUSSION AND CONCLUSIONS

The rheology of dense frictional suspensions determined by the extensive numerical simulations presented here displays continuous and discontinuous shear thickening and, at sufficiently large  $\phi$ , shear-induced jamming. All of these behaviors are predicted by the model structure of Wyart and Cates<sup>24</sup>. We provide a thorough examination of the influence of the interparticle friction coefficient on the jamming fraction in the near-hard-sphere limit. We find that the approach to the jamming point of both the shear and normal stresses scale well with volume fraction as  $(\phi_J - \phi)^{-2}$  for either the lubricated or frictional case. The comprehensive and coherent database from these simulations allows us to make detailed comparisons against a constitutive model incorporating stress-dependent frictional effects in dense suspensions.

We find that a model defined by three parameters — solid volume fraction  $\phi$ , dimensionless stress  $\tilde{\sigma} = \sigma/\sigma_0$  and interparticle friction coefficient  $\mu$  — captures well the extreme rate-dependence of the rheology of these materials. Here  $\sigma_0 = F_0/6\pi a^2$  is a stress scale determined by a stabilizing repulsive force of magnitude  $F_0$  at contact for particles of radius  $a$ . The central concept is that this stress scale divides the material response into low stress and high stress regions: when the stress is small,  $\tilde{\sigma} \ll 1$ , particle surfaces remain separated by lubrication films and the viscosity and normal stresses are relatively small. When the stress overwhelms the repulsive force, i.e., when  $\tilde{\sigma} \gg 1$ , frictional contacts dominate and the rheological functions are much larger. This leads to two

limiting jamming fractions:  $\phi_J^0$  in the frictionless states at low stress, and  $\phi_J(\mu) < \phi_J^0$  at high stress. A stress-dependent jamming fraction  $\phi_m(\tilde{\sigma}, \mu)$  can be defined by interpolating between these two jamming fractions as a function of the applied stress, as shown by (8a), in the manner proposed by Wyart and Cates<sup>24</sup> using the fraction of frictional contacts. The divergence of the stresses approaching the interpolated jamming fraction  $\phi_m$  follows the form of the two limits, with the stresses growing as  $(\phi_m - \phi)^{-2}$ .

Based on these concepts, a constitutive model for dense frictional suspensions in steady simple shear flow has been proposed. Comparison of the model predictions, e.g. relative viscosity  $\eta_r(\phi, \tilde{\sigma}, \mu)$ , agree well over the full range of parameters with the simulations reported here. The overall behavior is described by a flow-state diagram given in Fig. 6. This diagram, particularly in the  $\phi$  -  $\tilde{\sigma}$  plane, displays the various regions of material behavior obtainable at a fixed value of  $\mu$ . At smaller  $\phi$ , the material shear thickens continuously (CST), while above a critical solid fraction  $\phi_C$  the shear thickening becomes discontinuous. We find two regimes of DST: (i) a pure DST regime between two *flowing* states for  $\phi_C < \phi < \phi_J(\mu)$ , and (ii) a DST-SJ regime where with increase of  $\tilde{\sigma}$ , DST gives way to shear-jamming for  $\phi_J(\mu) < \phi < \phi_J^0$ . In both the scenarios (i) and (ii), upon increase in  $\tilde{\sigma}$  the suspension under shear goes through CST over a range of stress before entering DST. With increasing  $\mu$ ,  $\phi_J(\mu)$  decreases, and as a consequence the range of  $\phi$  over which shear jamming is observed, i.e.  $\phi_J(\mu) < \phi < \phi_J^0$ , increases. The range of volume fraction  $\phi_C < \phi < \phi_J(\mu)$  for which DST is observed also broadens with increase of  $\mu$ . The onset stress to observe the shear-jammed state decreases with increase in  $\phi$ , and  $\tilde{\sigma}_J \rightarrow 0$  as  $\phi \rightarrow \phi_J^0$ .

Once the key parameters in the model are fitted the

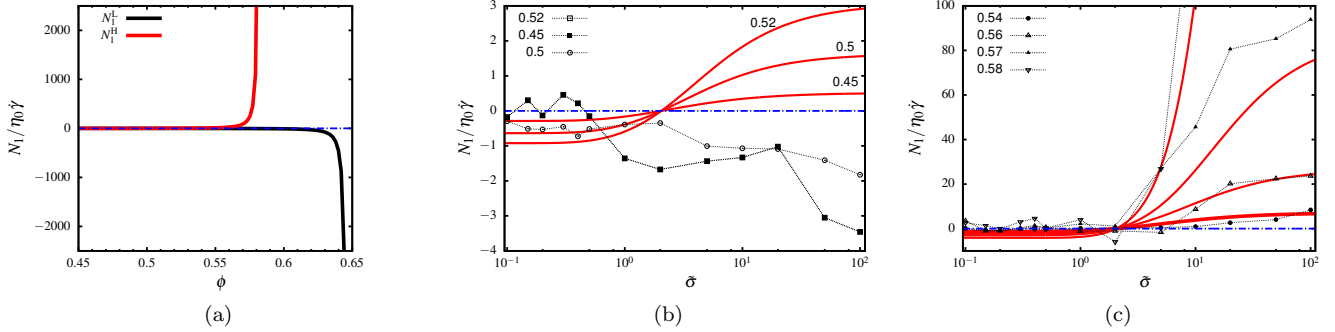


FIG. 8. (a) Divergence of the lubrication and frictional contributions of  $N_1$ . The lubrication part is negative and diverges at  $\phi_J^0$ , while the frictional part is positive and diverges at  $\phi_J(\mu)$ , and  $K_1^0 = 0.055$ ,  $K_1(\mu) = 0.045$  (b)  $N_1/\eta_0\dot{\gamma}(\phi, \tilde{\sigma})$  plotted as a function of  $\tilde{\sigma} = \sigma/\sigma_0$  for volume fraction  $\phi < 0.54$ . (c)  $N_1/\eta_0\dot{\gamma}(\phi, \tilde{\sigma})$  plotted as a function of  $\tilde{\sigma} = \sigma/\sigma_0$  for high volume fraction  $\phi \geq 0.54$ . Symbols and dashed lines indicate the simulation data while solid lines are predictions from (11a).

entire flow-state diagram can be constructed. To achieve the fitting, a measure of the two jamming volume fractions ( $\phi_J^0$  and  $\phi_J(\mu)$ ) and a stress ramp  $\eta_r(\sigma)$  at one volume fraction  $\phi$  are required. The two jamming fractions can also be extracted from stress ramps at several  $\phi$  provided these are sufficiently concentrated.

Finally, we expect that the formulation of the model itself should be robust to changes of particle properties such as polydispersity, particle shape, and other surface properties. However, the values of the parameters such as  $\phi_J$  are known to be sensitive to these details<sup>45–47</sup>. Extending this framework to Brownian<sup>16</sup> and cohesive suspensions<sup>48</sup>, where a strong shear thinning and yielding behavior are observed, would be valuable.

## VI. ACKNOWLEDGMENTS

Our code makes use of the CHOLMOD library by Tim Davis (<http://faculty.cse.tamu.edu/davis/suitesparse.html>) for direct Cholesky factorization of the sparse resistance matrix. This work was supported, in part, under National Science Foundation Grants CNS-0958379, CNS-0855217, ACI-1126113 and the City University of New York High Performance Computing Center at the College of Staten Island. JFM was supported by NSF 1605283.

- <sup>1</sup>J. Mewis and N. J. Wagner, *Colloidal Suspension Rheology* (Cambridge University Press, 2011).
- <sup>2</sup>E. Guazzelli and J. F. Morris, *A Physical Introduction to Suspension Dynamics* (Cambridge University Press, 2011).
- <sup>3</sup>M. M. Denn and J. F. Morris, “Rheology of non-Brownian suspensions,” *Annu. Rev. Chem. Biomol. Eng.* **5** (2014).
- <sup>4</sup>I. R. Peters, S. Majumdar, and H. M. Jaeger, “Direct observation of dynamic shear jamming in dense suspensions,” *Nature* **532**, 214–217 (2016).
- <sup>5</sup>A. B. Metzner and M. Whitlock, “Flow behavior of concentrated (dilatant) suspensions,” *Trans. Soc. Rheol.* **2**, 239–253 (1958).
- <sup>6</sup>H. A. Barnes, “Shear-thickening (“dilatancy”) in suspensions of nonaggregating solid particles dispersed in Newtonian liquids,” *J. Rheol.* **33**, 329–366 (1989).
- <sup>7</sup>E. Brown and H. M. Jaeger, “Shear thickening in concentrated suspensions: phenomenology, mechanisms and relations to jamming,” *Rep. Prog. Phys.* **77**, 046602 (2014).
- <sup>8</sup>N. Fernandez, R. Mani, D. Rinaldi, D. Kadau, M. Mosquet, H. Lombois-Burger, J. Cayer-Barrioz, H. J. Herrmann, N. D. Spencer, and L. Isa, “Microscopic mechanism for shear thickening of non-Brownian suspensions,” *Phys. Rev. Lett.* **111**, 108301 (2013).
- <sup>9</sup>Z. Pan, H. de Cagny, B. Weber, and D. Bonn, “S-shaped flow curves of shear thickening suspensions: Direct observation of frictional rheology,” *Phys. Rev. E* **92**, 032202 (2015).
- <sup>10</sup>B. M. Guy, M. Hermes, and W. C. K. Poon, “Towards a unified description of the rheology of hard-particle suspensions,” *Phys. Rev. Lett.* **115**, 088304 (2015).
- <sup>11</sup>C. Clavaud, A. Bérut, B. Metzger, and Y. Forterre, “Revealing the frictional transition in shear-thickening suspensions,” *Proc. Natl. Acad. Sci. U.S.A.* **114**, 5147–5152 (2017).
- <sup>12</sup>J. Comtet, G. Chatté, A. Niguès, L. Bocquet, A. Siria, and A. Colin, “Pairwise frictional profile between particles determines discontinuous shear thickening transition in non-colloidal suspensions,” *Nat. Comm.* **8**, 15633 (2017).
- <sup>13</sup>R. Seto, R. Mari, J. F. Morris, and M. M. Denn, “Discontinuous shear thickening of frictional hard-sphere suspensions,” *Phys. Rev. Lett.* **111**, 218301 (2013).
- <sup>14</sup>C. Heussinger, “Shear thickening in granular suspensions: interparticle friction and dynamically correlated clusters,” *Phys. Rev. E* **88**, 050201(R) (2013).
- <sup>15</sup>R. Mari, R. Seto, J. F. Morris, and M. M. Denn, “Shear thickening, frictionless and frictional rheologies in non-Brownian suspensions,” *J. Rheol.* **58**, 1693–1724 (2014).
- <sup>16</sup>R. Mari, R. Seto, J. F. Morris, and M. M. Denn, “Nonmonotonic flow curves of shear thickening suspensions,” *Phys. Rev. E* **91**, 052302 (2015).
- <sup>17</sup>C. Ness and J. Sun, “Shear thickening regimes of dense non-Brownian suspensions,” *Soft Matter* **12**, 914–924 (2016).
- <sup>18</sup>J. R. Melrose and R. C. Ball, “The pathological behaviour of sheared hard spheres with hydrodynamic interactions,” *Europhys. Lett.* **32**, 535–540 (1995).
- <sup>19</sup>L. E. Silbert, “Jamming of frictional spheres and random loose packing,” *Soft Matter* **6**, 2918–2924 (2010).
- <sup>20</sup>M. Otsuki and H. Hayakawa, “Critical scaling near jamming transition for frictional granular particles,” *Phys. Rev. E* **83**, 051301 (2011).
- <sup>21</sup>M. P. Ciamarra, R. Pastore, M. Nicodemi, and A. Coniglio, “Jamming phase diagram for frictional particles,” *Phys. Rev. E* **84**, 041308 (2011).
- <sup>22</sup>S. Chialvo, J. Sun, and S. Sundaresan, “Bridging the rheology of granular flows in three regimes,” *Phys. Rev. E* **85**, 021305 (2012).

<sup>23</sup>I. Bashkirtseva, A. Y. Zubarev, L. Y. Iskakova, and L. Ryashko, “On rheophysics of high-concentrated suspensions,” *Colloid Journal* **71**, 446–454 (2009).

<sup>24</sup>M. Wyart and M. E. Cates, “Discontinuous shear thickening without inertia in dense non-Brownian suspensions,” *Phys. Rev. Lett.* **112**, 098302 (2014).

<sup>25</sup>M. Neuville, G. Bossis, J. Persello, O. Volkova, P. Boustingorry, and M. Mosquet, “Rheology of a gypsum suspension in the presence of different superplasticizers,” *Journal of Rheology* **56**, 435–451 (2012).

<sup>26</sup>M. Hermes, B. M. Guy, W. C. K. Poon, G. Poy, M. E. Cates, and M. Wyart, “Unsteady flow and particle migration in dense, non-Brownian suspensions,” *J. Rheol.* **60**, 905–916 (2016).

<sup>27</sup>J. F. Morris and F. Boulay, “Curvilinear flows of noncolloidal suspensions: The role of normal stresses,” *J. Rheol.* **43**, 1213–1237 (1999).

<sup>28</sup>J. Dong and M. Trulsson, “Discontinuous shear thickening of dense suspensions under confining pressure,” arXiv:1701.06934 [cond-mat] (2017).

<sup>29</sup>R. Mari, R. Seto, J. F. Morris, and M. M. Denn, “Discontinuous shear thickening in Brownian suspensions by dynamic simulation,” *Proc. Natl. Acad. Sci. U.S.A.* **112**, 15326–15330 (2015).

<sup>30</sup>C. D. Cwalina and N. J. Wagner, “Material properties of the shear-thickened state in concentrated near hard-sphere colloidal dispersions,” *J. Rheol.* **58**, 949–967 (2014).

<sup>31</sup>R. C. Ball and J. R. Melrose, “A simulation technique for many spheres in quasi-static motion under frame-invariant pair drag and Brownian forces,” *Phys. A* **247**, 444–472 (1997).

<sup>32</sup>D. J. Jeffrey, “The calculation of the low Reynolds number resistance functions for two unequal spheres,” *Phys. Fluids A* **4**, 16–29 (1992).

<sup>33</sup>P. Mills and P. Snabre, “Apparent viscosity and particle pressure of a concentrated suspension of non-Brownian hard spheres near the jamming transition,” *Eur. Phys. J. E* **30**, 309–316 (2009).

<sup>34</sup>F. Boyer, É. Guazzelli, and O. Pouliquen, “Unifying suspension and granular rheology,” *Phys. Rev. Lett.* **107**, 188301 (2011).

<sup>35</sup>J. Mewis and N. J. Wagner, *Colloidal Suspension Rheology* (Cambridge University Press, 2011).

<sup>36</sup>T. N. Phung, J. F. Brady, and G. Bossis, “Stokesian dynamics simulation of Brownian suspensions,” *J. Fluid Mech.* **313**, 181–207 (1996).

<sup>37</sup>M. E. Cates, J. P. Wittmer, J.-P. Bouchaud, and P. Claudin, “Jamming, force chains, and fragile matter,” *Phys. Rev. Lett.* **81**, 1841–1844 (1998).

<sup>38</sup>D. R. Foss and J. F. Brady, “Structure, diffusion and rheology of Brownian suspensions by Stokesian dynamics simulation,” *J. Fluid Mech.* **407**, 167–200 (2000).

<sup>39</sup>J. R. Royer, D. L. Blair, and S. D. Hudson, “Rheological signature of frictional interactions in shear thickening suspensions,” *Phys. Rev. Lett.* **116**, 188301 (2016).

<sup>40</sup>M. Lee, M. Alcoutabi, J. J. Magda, C. Dibble, M. J. Solomon, X. Shi, and G. B. McKenna, “The effect of the shear-thickening transition of model colloidal spheres on the sign of  $n_1$  and on the radial pressure profile in torsional shear flows,” *J. Rheol.* **50**, 293–311 (2006).

<sup>41</sup>D. Lootens, H. van Damme, Y. Hémar, and P. Hébraud, “Dilatant flow of concentrated suspensions of rough particles,” *Phys. Rev. Lett.* **95**, 268302 (2005).

<sup>42</sup>B. J. Maranzano and N. J. Wagner, “The effects of particle size on reversible shear thickening of concentrated colloidal dispersions,” *J. Chem. Phys.* **114**, 10514–527 (2001).

<sup>43</sup>R. J. Larsen, J.-W. Kim, C. F. Zukoski, and D. A. Weitz, “Elasticity of dilatant particle suspensions during flow,” *Phys. Rev. E* **81**, 011502 (2010).

<sup>44</sup>T. Dbouk, L. Lobry, and E. Lemaire, “Normal stresses in concentrated non-Brownian suspensions,” *J. Fluid Mech.* **715**, 239–272 (2013).

<sup>45</sup>M. van Hecke, “Jamming of soft particles: geometry, mechanics, scaling and isostaticity,” *J. Phys. Condens. Matter* **22**, 033101 (2009).

<sup>46</sup>A. J. Liu and S. R. Nagel, “Granular and jammed materials,” *Soft Matter* **6**, 2869–2870 (2010).

<sup>47</sup>A. J. Liu and S. R. Nagel, “The jamming transition and the marginally jammed solid,” *Annu. Rev. Condens. Matter Phys.* **1**, 347–369 (2010).

<sup>48</sup>S. Pednekar, J. Chun, and J. F. Morris, “Simulation of shear thickening in attractive colloidal suspensions,” *Soft Matter* **13**, 1773–1779 (2017).

## VII. SUPPLEMENTARY INFORMATION

### A. Effect of friction on normal stresses

Normal stresses ( $\Pi/\eta_0\dot{\gamma}$  and  $N_2/\eta_0\dot{\gamma}$ ) obtained from (9) are presented in Figs. 9 and 10 along with simulation data for different values of  $\mu$ . The model is in excellent agreement with the data. For a given volume fraction  $\phi$ , both  $\Pi/\eta_0\dot{\gamma}$  and  $|N_2/\eta_0\dot{\gamma}|$  increase with  $\mu$ .

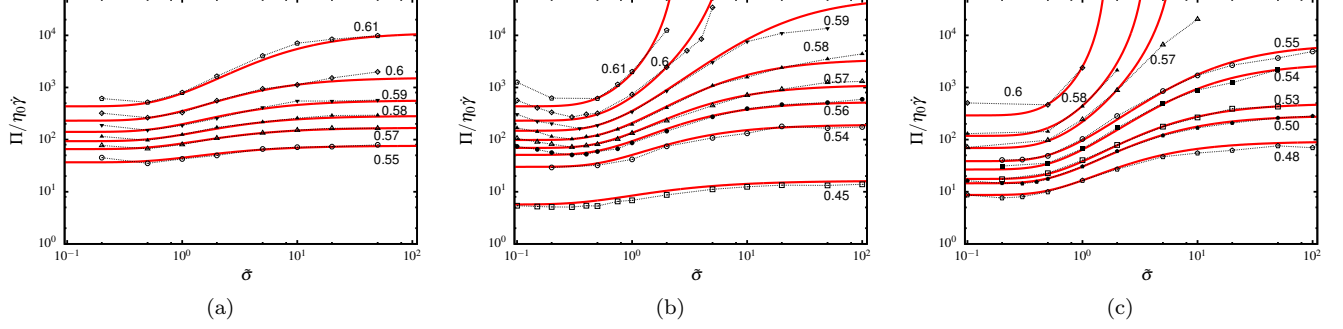


FIG. 9. Steady state particle pressure  $\Pi/\eta_0\dot{\gamma}$  plotted against applied stress  $\tilde{\sigma} = \sigma/\sigma_0$  for  $\mu =$  (a) 0.2, (b) 0.5, (c) 10 for several values of volume fractions as mentioned. Symbols and dashed lines indicate the simulation data while solid lines are predictions from (9b).

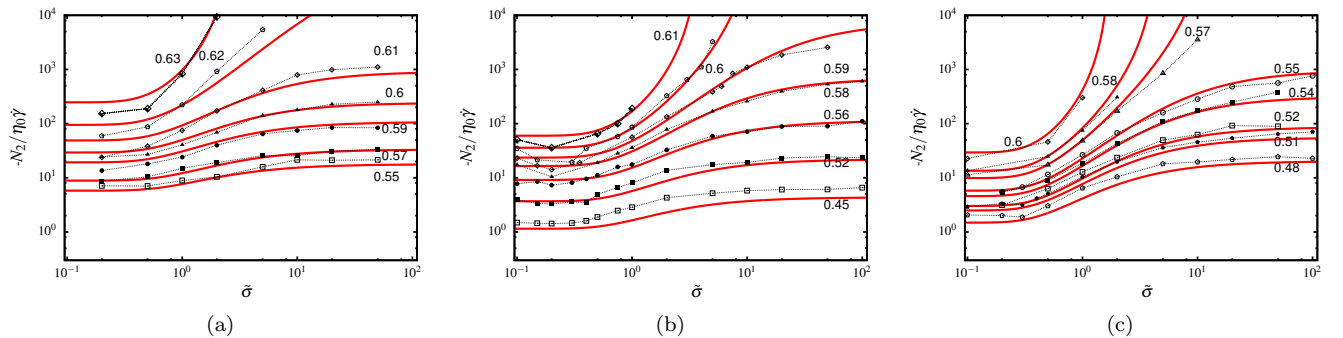


FIG. 10. Steady state second normal stress difference  $N_2/\eta_0\dot{\gamma}$  plotted against applied stress  $\tilde{\sigma} = \sigma/\sigma_0$  for  $\mu =$  (a) 0.2, (b) 0.5, (c) 10 for several values of volume fractions as mentioned. Symbols and dashed lines indicate the simulation data while solid lines are predictions from (9c).